Enhanced Dynamic Operation of Heavily Saturated IPMSM in Signal-Injection Sensorless Control

Inhwi Hwang
Dept. of Electrical and Computer Engineering
Seoul National University
Seoul, Republic of Korea
snuhwi96@gmail.com

Yong-Cheol Kwon
Dept. of Electrical and Computer Engineering
Seoul National University
Seoul, Republic of Korea
dydcjfe@gmail.com

Seung-Ki Sul
Dept. of Electrical and Computer Engineering
Seoul National University
Seoul, Republic of Korea
sulsk@snu.ac.kr

***Abstract*—This paper proposes a signal-injection sensorless control (SISC) algorithm with enhanced dynamic performance for heavily saturated interior permanent-magnet synchronous motors (IPMSMs). In the proposed method, not only tilting the high frequency (HF) voltage injection angle but also titling the *q*-axis for the current component from the injection is employed to enlarge the magnitude of HF current signal and to improve the position tracking capability. The performance of the proposed method is verified by carefully designed experiments in dynamic SISC operations. The performance for the step torque reference following has been enhanced conspicuously.**

Keywords—Signal-injection sensorless control (SISC), permanent-magnet synchronous motor, finite element analysis (FEA), convergence analysis.

I. INTRODUCTION

In traction applications, sensorless control algorithms have been considered a backup algorithm against the sudden failure of the position sensor. The sensorless control algorithms can be divided into the signal-injection sensorless control (SISC) based on intentionally injected high-frequency (HF) voltage and its induced current [1], and the model-based sensorless control [2]-[3] that utilizes fundamental voltage/current components used for control of the motor. Interestingly, it has already been known that the position estimation capability of SISC can be lost in heavy-loading condition [4]-[5]. In this condition, the iron core of interior permanent-magnet synchronous motors (IPMSM) could be highly saturated by the magnetic flux induced by the stator current. Thus the spatial magnetic flux distribution would be reshaped undesirably.

For this reason, sensorless operation in the higher torque region was considered to be impossible with the conventional SISC. Therefore, it was essential to determine the maximum operable torque point of SISC [6]-[8], and there were also efforts to change the shape of a motor to overcome the torque limitation [9]-[10]. In addition, input disturbance analysis of SISC observer was also conducted. It was identified that the main factors of the disturbance were the dead-time and the voltage drop of the switching element [11]-[12].

Some methods have been proposed for SISC in the high torque region. For instance, compensation method of the offset error in the position tracking was proposed in [13]-[16]. Also, it had been proposed that HF voltage was injected not in the *d*-axis of the estimated rotor reference frame (ERRF) but the *d*-axis of the tilted reference frame in [17]. Moreover, the *q*-axis of a tilted reference frame is exploited to get an error signal. The SISC performance was improved by tilting the current reference without tilting the signal injection angle in [18]. These methods [17]-[18] could conspicuously improve the torque capability of IPMSM in SISC. However, the position tracking with the above methods can become unstable or marginally stable in highly dynamic operating condition since they mainly focus on the steady-state stability of SISC.

Similar methodologies were also employed in [19]-[20]. The authors in [19] took the effect of cross-saturation into account to eliminate position tracking error by adding HF differential current component of *d*-axis to that of *q*-axis and using it as an error signal. However, they did not consider the inductance variation according to the position error. In contrast, authors in [20] dealt with the change in inductance according to the position error, and they also make use of injection tiliting method in heavy load condition. However, they all ignored the impact of spatial harmonics on HF inductance in a highly saturated condition.

This paper proposes a SISC method that can improve the position tracking characteristics in dynamic transient by maximizing effective signal embedding the position information. In the proposed method, injection angle titling and additional current component of *d*-axis to that of *q*-axis are exploited to enlarge the magnitude of the effective signal. It is equivalent to additional tilting of *q*-axis where the current ripple from the injection is observed. Furthermore, the newly defined variable gain connecting the HF current to the angle error, the input to the angle tracking observer, could reflect the variation of dynamic inductances in the heavily saturated IPMSM.

This work was supported by the Seoul national university Electric Power Research Institute (SEPRI).

978-1-7281-9387-8/22/$31.00 ©2022 IEEE

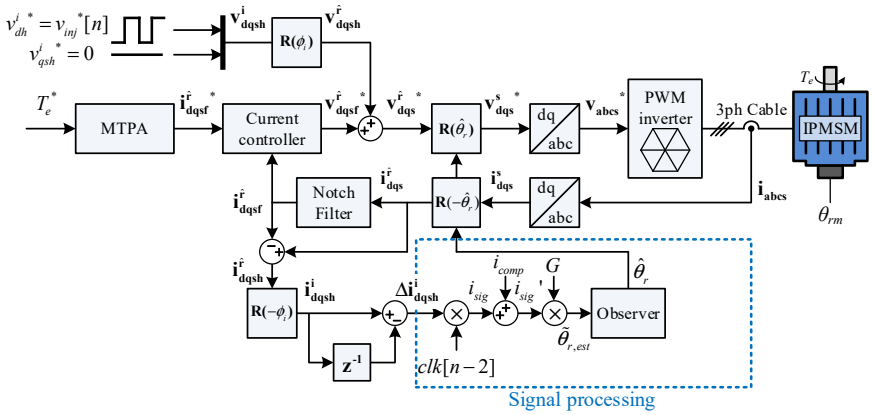

Fig. 1. Conventional SISC system block diagram [17].

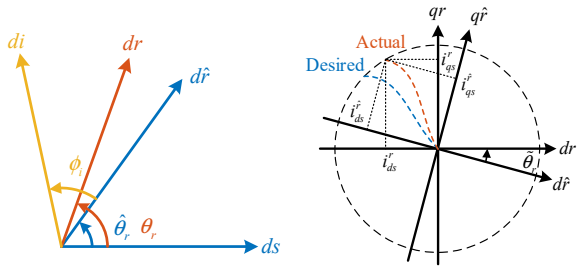

(a) (b)

Fig. 2. (a) Definition of angles and axes. (b) Actual and desired MTPA curve with respect to position error.

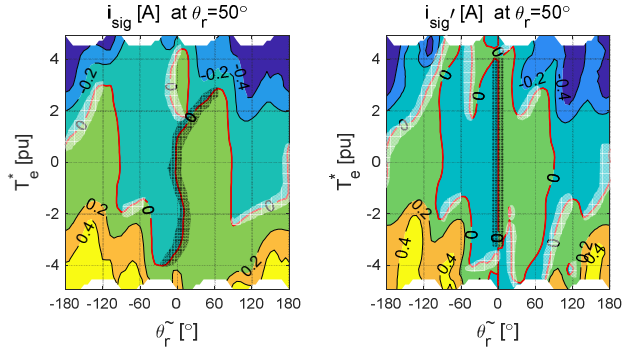

(a) (b)

Fig. 3. (a) Contour maps of i_{sig} and (b) i_{sig}' ($\theta_r = 50°$, and $\phi_i = 0°$).

Table I. Specifications of target IPM (FEA).

Pole/Slot	6/12
Rated Torque	1.17 Nm
Rated Current	4.03 A_{peak}
λ_f	63 mWb-t
L_{ds}	7.13 mH
L_{qs}	11.04 mH

II. Conventional Method

A. Signal-Injection Sensorless Control with Ancillary Injection Reference Frame

The HF voltage equation of IPMSM can be formulated as follows:

$$\begin{bmatrix} v^r_{dsh} \\ v^r_{qsh} \end{bmatrix} = \mathbf{L_h} \frac{d}{dt} \begin{bmatrix} i^r_{dsh} \\ i^r_{qsh} \end{bmatrix} = \begin{bmatrix} L_{dh} & L_{dqh} \\ L_{qdh} & L_{qh} \end{bmatrix} \frac{d}{dt} \begin{bmatrix} i^r_{dsh} \\ i^r_{qsh} \end{bmatrix} = \begin{bmatrix} \frac{\partial \lambda^r_{ds}}{\partial i^r_{ds}} & \frac{\partial \lambda^r_{ds}}{\partial i^r_{qs}} \\ \frac{\partial \lambda^r_{qs}}{\partial i^r_{ds}} & \frac{\partial \lambda^r_{qs}}{\partial i^r_{qs}} \end{bmatrix} \frac{d}{dt} \begin{bmatrix} i^r_{dsh} \\ i^r_{qsh} \end{bmatrix}. \quad (1)$$

In (1), v stands for voltage, i for current, L for inductance, and λ for magnetic flux. The superscript 'r' means the rotor reference frame (RRF), the subscript 's' stands for the stator component, and 'h' for the HF component. $\mathbf{L_h}$ is the dynamic inductance matrix, the partial derivative of the magnetic flux regarding the current. Eq. (1) holds under the assumption that the HF resistance is negligible compared to the HF reactance. i^r_{dsh} and i^r_{qsh} are obtained from the notch filter output used for SISC signal processing.

Fig. 1 shows a control block diagram of the conventional SISC system [17] that is the background of this paper. In this paper, square-wave type voltage injection [1] is used for SISC.

Fig. 2 (a) depicts various angles and axes for discussion in this paper. In the figure, θ_r stands for the rotor position, $\hat{\theta}_r$ for the estimated rotor position, and $\tilde{\theta}_r$ for the position error. Note that the actual current is not the same as the current reference in Fig. 2 (b) if $\tilde{\theta}_r$ is not zero. The actual operating point changes as $\tilde{\theta}_r$ varies, which inevitably results in the variation of the HF inductance and torque discrepancy. In addition, there is an ancillary injection angle, ϕ_i, in Fig. 2 (a). ϕ_i is the ancillary injection angle defined in [17]. 'ds' is the d-axis of stationary reference frame, 'dr' is that of RRF, '$d\hat{r}$' is that of ERRF, 'di' is that of ancillary injection reference frame (AIRF). The superscript 'i' represents AIRF.

In AIRF, HF injection voltage reference $\mathbf{v}^{i}_{\mathbf{dqsh}}{}^{*}$ can be expressed as follows:

$$\mathbf{v}^{i}_{\mathbf{dqsh}}{}^{*}[n] = \begin{bmatrix} v_{inj}{}^{*}[n] \\ 0 \end{bmatrix} = \begin{bmatrix} V_h \cdot clk[n] \\ 0 \end{bmatrix}, \quad (2)$$

where V_h is the amplitude of injection voltage and

$$clk[n] = \begin{cases} 1 & \text{when n is odd} \\ -1 & \text{else} \end{cases} \quad (3)$$

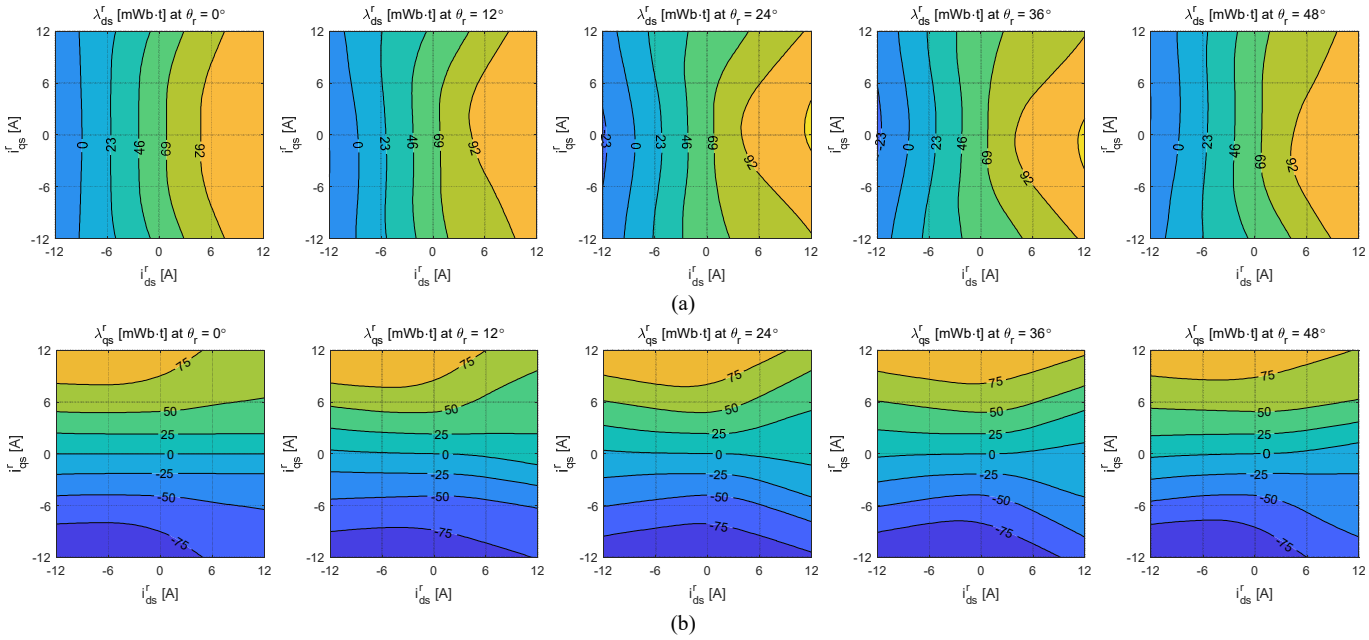

Fig. 4. (a) λ_{ds}^{r} and (b) λ_{qs}^{r} maps of IPM under test (FEA).

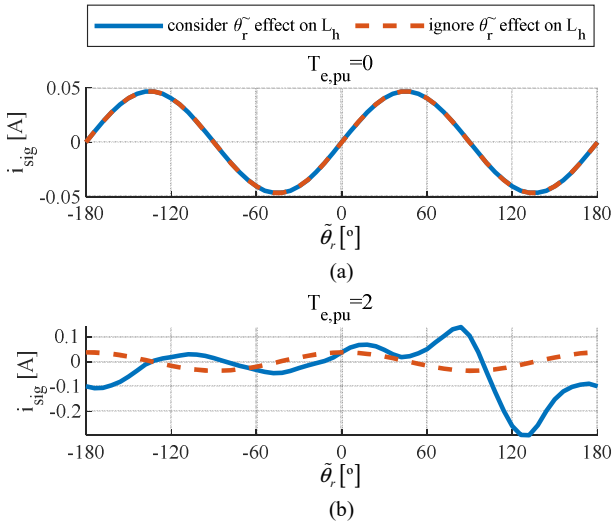

Fig. 5. (a) i_{sig} curves of IPMSM according to $\tilde{\theta}_r$ with T_e^* = 0 pu, (b) 2 pu (θ_r = 0°, and ϕ_i = 0°).

is a pulsating signal with the value of ±1. $\mathbf{v}_{\mathbf{dqsh}}^{\mathbf{i}}{}^{*}$ is applied to the motor through the inverter using pulse width modulation (PWM). The current variation of HF current component at n sampling instant in AIRF induced by the corresponding HF voltage, $\Delta\mathbf{i}_{\mathbf{dqsh}}^{\mathbf{i}}[n] \equiv \mathbf{i}_{\mathbf{dqsh}}^{\mathbf{i}}[n] - \mathbf{i}_{\mathbf{dqsh}}^{\mathbf{i}}[n-1]$, can be derived as

$$\Delta\mathbf{i}_{\mathbf{dqsh}}^{\mathbf{i}}[n] = \begin{bmatrix} \Delta i_{dsh}^{i}[n] \\ \Delta i_{qsh}^{i}[n] \end{bmatrix} = \begin{bmatrix} I_\Sigma + I_\Delta \cos\left(2\tilde{\theta}_r - 2\phi_\Delta - 2\phi_i\right) \\ I_\Delta \sin\left(2\tilde{\theta}_r - 2\phi_\Delta - 2\phi_i\right) \end{bmatrix} \cdot clk[n-2], \quad (4)$$

where

$$I_\Sigma = \frac{V_h T_s \Sigma L_h}{L_{dh}L_{qh} - L_{dqh}^{\ 2}}, \quad (5)$$

$$I_\Delta = \frac{V_h T_s \sqrt{L_{dqh}^{\ 2} + \Delta L_h^{\ 2}}}{L_{dh}L_{qh} - L_{dqh}^{\ 2}}, \quad (6)$$

$$\text{and } \phi_\Delta = \frac{1}{2}\text{atan2}\left(L_{dqh}, -\Delta L_h\right). \quad (7)$$

In (5)-(7), $\Sigma L_h \equiv \frac{1}{2}\left(L_{dh} + L_{qh}\right)$ and $\Delta L_h \equiv \frac{1}{2}\left(L_{dh} - L_{qh}\right)$. '*clk*' should be removed to extract the angular error information from $\Delta\mathbf{i}_{\mathbf{dqsh}}^{\mathbf{i}}$. For this, $\Delta i_{qsh}^{i}[n]$ in (4) is multiplied by *clk*[n] to obtain i_{sig} as follows:

$$i_{sig} = \Delta i_{qsh}^{i} \cdot clk[n]. \quad (8)$$

After that, the following compensation current (i.e., i_{comp}) was introduced to eliminate the offset error. i_{comp} is expressed as follows:

$$i_{comp}\left(T_e^*, \hat{\theta}_r\right) = -i_{sig}\left(T_e^*, \tilde{\theta}_r = 0, \theta_r = \hat{\theta}_r\right), \quad (9)$$

where T_e^* means a torque command. Compensation current, i_{comp}, is added to i_{sig} to get i_{sig}' as follows:

$$i_{sig}' = i_{sig} + i_{comp}. \quad (10)$$

Dividing i_{sig}' by $2I_\Delta$, $\tilde{\theta}_{r,est}[n]$ can be obtained as follows:

$$\tilde{\theta}_{r,est}[n] = \frac{i_{sig}'}{2I_\Delta}. \quad (11)$$

$\tilde{\theta}_{r,est}[n]$ is used as the input to the observer.

Fig. 3 depicts the contours of i_{sig} and i_{sig}' with θ_r = 50°. The red lines in the contours indicate the zero-level points. In the figure, the major convergence points are the points that reach out from the desired convergence point with T_e^*=0, which is near $\tilde{\theta}_r = 0$. The major convergence points are overlaid with gray shadow on the top of the red line in Fig. 3. The other convergence points are the minor ones overlaid with white shadow on the top of the red line in Fig. 3. The major convergence point in Fig. 3 (a) goes far from the $\tilde{\theta}_r = 0$ line as T_e^* increases due to the large variation of HF inductance. However, the major convergence points can be manipulated to the desired point, as shown in Fig. 3 (b) by using i_{comp} [13]. This method is essential to keep zero error in SISC even if the ancillary injection angle is tilted and the current component of *d*-axis is added to that of *q*-axis.

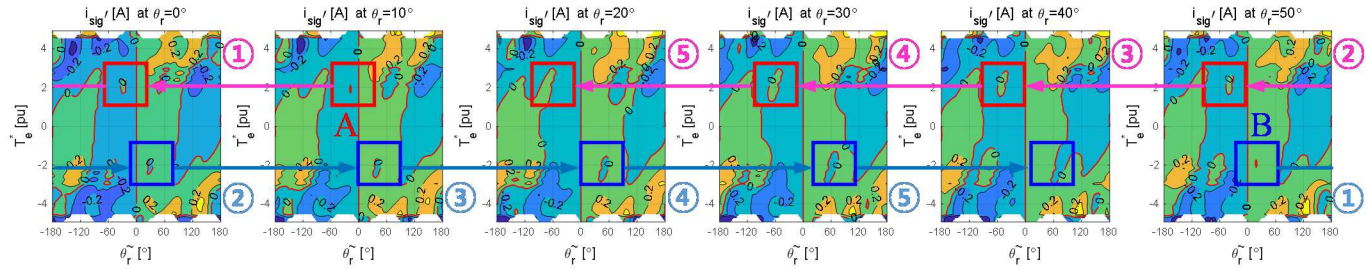

Fig. 6. Contour maps of i_{sig}' with conventional SISC method [17].

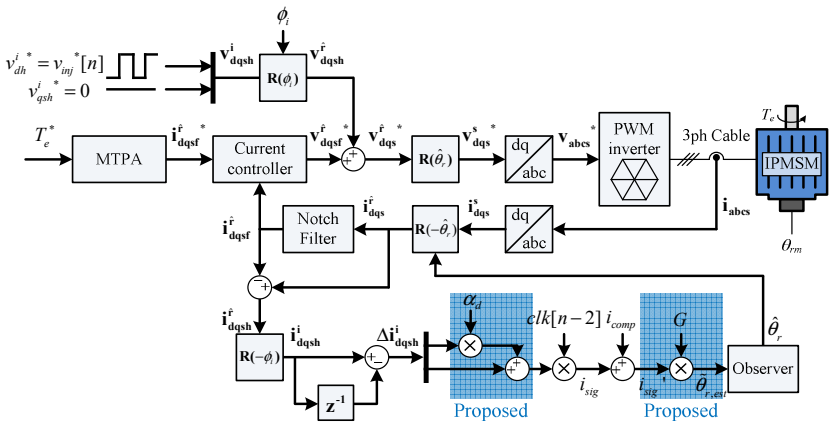

Fig. 7. Proposed SISC system block diagram.

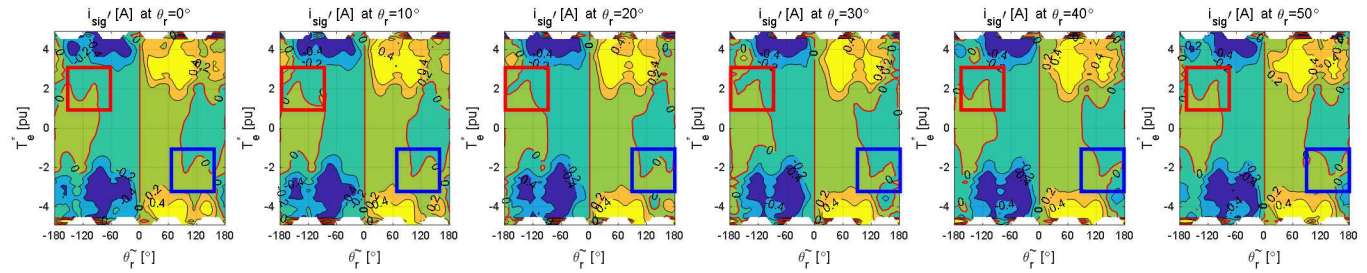

Fig. 8. Contour maps of i_{sig}' with proposed SISC.

Table I shows the specifications of IPMSM under test. Its characteristics are investigated through finite element analysis (FEA).

Fig. 4 shows λ_{ds}^r and λ_{qs}^r of IPMSM according to i_{ds}^r, i_{qs}^r, and θ_r. Because of the low-speed operation, loss components such as stator/rotor core losses and eddy current loss are not considered. Owing to 60º periodicity in spatial harmonics of the IPMSM, contours are shown for 0-48º rotor position in 12º step.

Fig. 5 demonstrates how the variation of HF inductance by $\tilde{\theta}_r$ variation affects i_{sig}. The orange line is drawn to fix the HF inductances with an operating point $\tilde{\theta}_r = 0°$, but the blue line is drawn considering the variation of HF inductance. With $T_e^* = 0$ pu, there is no difference between the two graphs. However, at $T_e^* = 2$ pu, they show a significant differences . This is because there is a distortion of flux distribution according to $\tilde{\theta}_r$ due to the large stator current.

B. Limitation of Conventional Method

In Fig. 6, contour maps of i_{sig}' show convergence characteristics of IPMSM in entire torque region for different rotor positions with the conventional method [17]. Red lines in the contour are points where i_{sig}' is zero. The major convergence points are on the $\tilde{\theta}_r = 0$ line, a set of target convergence points with a zero up-crossing condition. However, minor convergence points zero up-crossing but not on $\tilde{\theta}_r = 0$ line also exist. A convergence range is an interspace between boundaries of the zero down-crossings of i_{sig}', including a major convergence point. Within the convergence range, $\tilde{\theta}_r$ can converge toward the major convergence point by the negative feedback of the position tracking observer. However, according to Fig. 6, the minor convergence points are observed in the vicinity of the major convergence points with $T_e^* = \pm 2$ pu. The nearest minor convergence points from the $\tilde{\theta}_r = 0$ line exist in A (red box) and B (blue box) marked in Fig. 6. If $\tilde{\theta}_r$ converges to the minor convergence point in A due to disturbances, it would diverge along to the minor convergence point as the rotor rotates in negative direction with T_e^*=2 pu, as expressed with the pink arrows. The case with T_e^*=-2 pu can also be explained similarly with the blue arrows. Thus it is essential for $\tilde{\theta}_r$ not to fall into the minor convergence points for SISC operation.

III. Proposed Method

In this chapter, a SISC method is proposed to place the minor convergence points as far as possible from the $\tilde{\theta}_r = 0$ line by exploiting both ϕ_i and HF differential current of *d*-axis in AIRF.

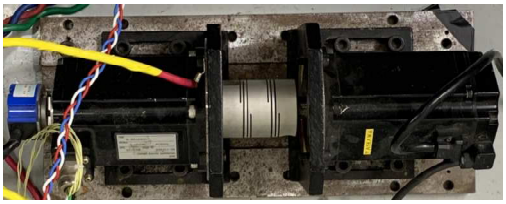

Fig. 9. Motor-generator set for experiment.

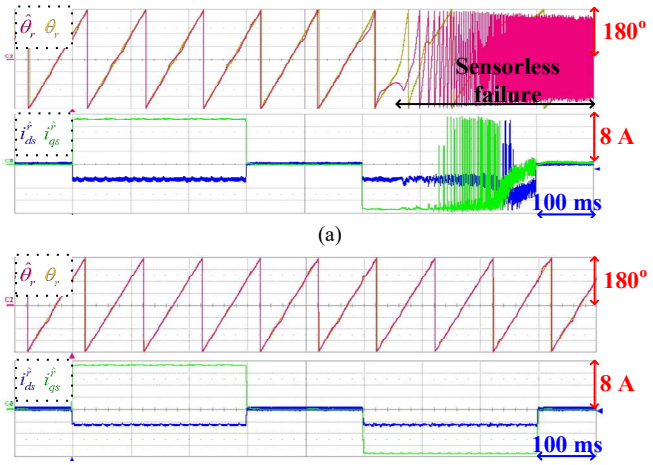

Fig. 10. Torque control experiment (current control bandwidth: 500 Hz): (a) Conventional SISC, (b) Proposed SISC with ±2 p.u. step torque command at 200 r/min.

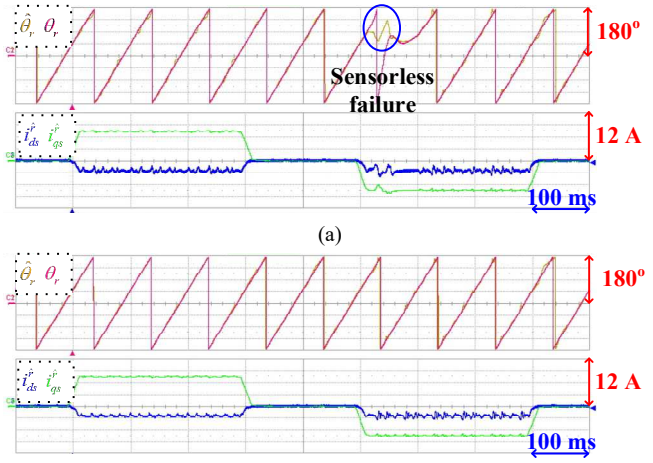

Fig. 11. Torque control experiment (current control bandwidth: 125 Hz): (a) Conventional SISC, (b) Proposed SISC with ±2 p.u. torque command of 100 p.u/s slew rate at 200 r/min.

Fig. 7 shows the signal processing method of the proposed SISC, and the signal processing block of the conventional SISC in Fig. 1 is replaced with that of Fig. 7. It has two significant differences compared to the conventional method [17]. First, the proposed method uses not only *q*-axis component of the HF current signal but also *d*-axis component in AIRF, which is newly proposed in this paper. i_{sig} in the proposed method can be obtained as follows:

$$i_{sig} = \left(\Delta i^{i}_{qsh} + \alpha_d \cdot \Delta i^{i}_{dsh}\right) \cdot clk[n] \tag{12}$$

where α_d is the gain of Δi^{i}_{dsh}. Since the major convergence point is manipulated by adding i_{comp} with (9), i_{sig}' itself can highly optimize convergence characteristics. Next, the gain G multiplied on i_{sig}' is newly defined as follows:

$$\tilde{\theta}_{r,est} = G \cdot i_{sig}' \tag{13}$$

where

$$G = \left(\frac{\partial i_{sig}'}{\partial \tilde{\theta}_r} \bigg|_{\tilde{\theta}_r = 0} \right)^{-1}. \tag{14}$$

i_{sig}' was linearly approximated to $\tilde{\theta}_{r,est}$ with gain of $\frac{1}{2I_\Delta}$ in the conventional method [17]-[18]. However, the slope of $\tilde{\theta}_{r,est}$ is affected not only by i_{comp} but also by α_d term, which is not fully considered in the conventional method. Therefore, the gain G defined as (14) is used in the proposed method instead of $\frac{1}{2I_\Delta}$. The gain could be evaluated by prior FEA. α_d should be set for manipulating minor convergence points as far as possible to guarantee convergence to the desired point, $\tilde{\theta}_r = 0°$, even in the dynamic condition.

In Fig. 8, it can be seen that the minor convergence points in the proposed method are further moved away from the $\tilde{\theta}_r = 0$ line than those in the conventional method in Fig. 6. Each red and blue square box indicates the minor convergence points with T_e^* = 2 pu and -2 pu each. Regardless of torque and rotor position, the distance between the $\tilde{\theta}_r = 0$ line and the minor convergence point is over 80° in the proposed method, which is distinctively larger than the conventional method. Therefore, the torque control in SISC would be much more robust to the disturbances from a severe load torque disturbance, measurement noise, and inverter nonlinearity.

The previous analysis was conducted with FEA data to extract proper ϕ_i and α_d. However, i_{comp} should be chosen by experiment. This is because i_{comp} calculated by FEA data can be different from the required i_{comp}, and this discrepancy of i_{comp} makes a large offset error. Therefore, FEA data are employed only for selecting ϕ_i and α_d. Based on these data, i_{comp} should be extracted from experimental results for more accurate compensation of i_{sig}.

IV. Experimental Results

Experiments are conducted to evaluate the dynamic performance of the conventional and the proposed SISC methods at high-loading conditions. In the experiments, the load machine is driven under speed control mode at 200 r/min. Fig. 9 shows the motor-generator (M-G) set used for the experiment.

In Fig. 10, the robustness of the proposed method against a step torque is verified. 2 pu torque command has been applied at 0.1 s, the command goes to zero at 0.4 s, and it goes down to – 2 pu at 0.6 s. After applying - 2 pu torque, $\hat{\theta}_r$ starts to diverge from t = 0.65 s and wholly loses position tracking capability in response to -2 pu step torque for the conventional method. However, in Fig. 10 (b), the sensorless algorithm works well thanks to the proposed SISC method.

In Fig. 11, within the transient, the $\hat{\theta}_r$ diverges at t = 0.63s and converges again soon after that with conventional SISC. It does not diverge permanently just because the load machine regulates the speed. However, it could cause a serious fault in

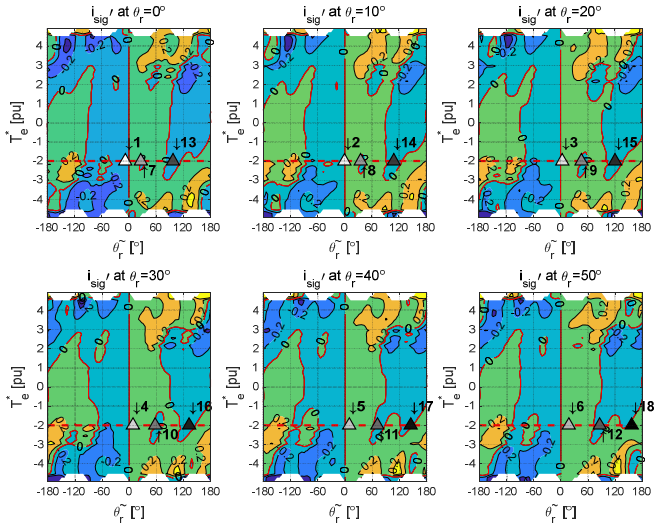

Fig. 12. $\tilde{\theta}_r$ trajectory with conventional SISC from t = 0.6 to 0.67 s in the experiment.

practical operating conditions where the load machine does not control the rotor. In contrast, the position is tracked under 7° position error with the proposed method, which is remarkably smaller than the conventional method.

Fig. 12 shows how the position error point moves on the i_{sig}' contour map in Fig. 10 (a). A white triangle indicates the initial operating point, and the face color of the triangle gets gradually darker as time goes by. Tagged numbers from 1 to 18 near the arrows represent some instants from 0.6 s to 0.67 s in the experiment with the conventional method. From points 1 to 6, $\tilde{\theta}_r$ is pushed to the minor convergence point due to the disturbance from the rapid current variation. After that, from point 7, $\tilde{\theta}_r$ is trapped at the minor convergence point. As the motor rotates in the positive direction, the trapped minor convergence point gradually moves away from 0°. After the motor rotates two times, at point 13, $\tilde{\theta}_r$ arrives at the more outlying convergence point than at point 7. After point 13, $\tilde{\theta}_r$ moves further away from 0° and eventually diverges. This divergence pattern fits in the trajectory depicted in Fig. 6.

V. Conclusion

This paper analyzes the convergence of IPMSM SISC. The proposed method uses injection tilting and current component of *d*-axis in addition to *q*-axis current component. A gain connecting the HF current to position error is newly defined to reflect the variation of the dynamic inductance of IPMSM under magnetic saturation. The proposed method solved the problem of the divergence of the position tracking observer under severely saturated IPMSM. The superiority of the proposed method was verified with the experiments. The robustness of the proposed method was also confirmed by applying stepwise torque. The observer tracked well the rotor position under highly saturated IPMSM in the proposed SISC.

Acknowledgement

This work was supported by the Seoul National University Electric Power Research Institute of the Korea Institute of Energy Technology Evaluation and Planning (KETEP) and the BK21 FOUR program of the Education and Research Program for Future ICT Pioneers in 2022, granted financial resource from the Ministry of Trade, Industry & Energy, Republic of Korea. The Institute of Engineering Research at Seoul National University provided research facilities for this work.

References

[1] Y. D. Yoon, S. K. Sul, S. Morimoto, and K. Ide, "High-bandwidth sensorless algorithm for AC machines based on square-wave-type voltage injection," *IEEE Trans. Ind. Appl.*, vol. 47, no. 3, pp. 1361-1370, May/Jun. 2011.

[2] S. Morimoto, K. Kawamoto, M. Sanada and Y. Takeda, "Sensorless control strategy for salient-pole PMSM based on extended EMF in rotating reference frame," *IEEE Trans. Ind. Appl.*, vol. 38, no. 4, pp. 1054-1061, Jul./Aug. 2002.

[3] N. Matsui, "Sensorless PM brushless DC motor drives," in *IEEE Trans. Ind. Electron.*, vol. 43, no. 2, pp. 300-308, Apr. 1996.

[4] Y. C. Kwon, J. Lee and S. K. Sul, "Recent advances in sensorless drive of interior permanent-magnet motor based on pulsating signal injection," *IEEE Trans. Emerg. Sel. Topics Power Electron.*, vol. 9, no. 6, pp. 6577-6588, Dec. 2021.

[5] D. Mingardi, M. Morandin, S. Bolognani and N. Bianchi, "On the Proprieties of the Differential Cross-Saturation Inductance in Synchronous Machines," in *IEEE Trans. Ind. Appl.*, vol. 53, no. 2, pp. 991-1000, Mar./Apr. 2017.

[6] M. Berto, L. Alberti, V. Manzolini and S. Bolognani, "Computation of self-sensing capabilities of synchronous machines for rotating high frequency voltage injection sensorless control," *IEEE Trans. Ind. Electron.*, vol. 69, no. 4, pp. 3324-3333, Apr. 2022.

[7] N. Bianchi, E. Fornasiero and S. Bolognani, "Effect of Stator and Rotor Saturation on Sensorless Rotor Position Detection," *IEEE Trans. Ind. Appl.*, vol. 49, no. 3, pp. 1333-1342, May/Jun. 2013.

[8] P. Guglielmi, M. Pastorelli and A. Vagati, "Cross-Saturation Effects in IPM Motors and Related Impact on Sensorless Control," *IEEE Trans. Ind. Appl.*, vol. 42, no. 6, pp. 1516-1522, Nov./Dec. 2006.

[9] N. Bianchi and S. Bolognani, "Influence of Rotor Geometry of an IPM Motor on Sensorless Control Feasibility," *IEEE Trans. Ind. Appl.*, vol. 43, no. 1, pp. 87-96, Jan./Feb. 2007.

[10] P. Sergeant, F. De Belie and J. Melkebeek, "Rotor Geometry Design of Interior PMSMs With and Without Flux Barriers for More Accurate Sensorless Control," *IEEE Trans. Ind. Electron.*, vol. 59, no. 6, pp. 2457-2465, Jun. 2012.

[11] Y. C. Kwon and S. K. Sul, "Reduction of Injection Voltage in Signal Injection Sensorless Drives Using a Capacitor-Integrated Inverter," *IEEE Trans. Power Electron.*, vol. 32, no. 8, pp. 6261-6274, Aug. 2017.

[12] C. E. Hwang, Y. Lee and S. K. Sul, "Analysis on Position Estimation Error in Position-Sensorless Operation of IPMSM Using Pulsating Square Wave Signal Injection," *IEEE Trans. Ind. Appl.*, vol. 55, no. 1, pp. 458-470, Jan./Feb. 2019.

[13] Y. Lee, Y. C. Kwon, S. K. Sul, N. A. Baloch, and S. Morimoto, "Compensation of position estimation error for precise position-sensorless control of IPMSM based on high-frequency pulsating voltage injection," in *Proc. IEEE Energy Convers. Congr. Expo.*, Oct. 2017, pp. 859-864.

[14] Y. Li, Z. Q. Zhu, D. Howe, C. M. Bingham and D. A. Stone, "Improved Rotor-Position Estimation by Signal Injection in Brushless AC Motors, Accounting for Cross-Coupling Magnetic Saturation," *IEEE Trans. Ind. Appl.*, vol. 45, no. 5, pp. 1843-1850, Sep./Oct. 2009.

[15] V. Manzolini and S. Bolognani, "On the Rotor Position Self-Sensing Capability of Reluctance and IPM Synchronous Motors," *IEEE Trans. Ind. Appl.*, vol. 56, no. 4, pp. 3755-3766, Jul./Aug. 2020.

[16] Z. Q. Zhu, Y. Li, D. Howe, and C. M. Bingham, "Compensation for rotor position estimation error due to cross-coupling magnetic saturation in signal injection based sensorless control of PM brushless AC motors," in *Proc. IEEE IEMDC*, 2007, vol. 1, pp. 208–213.

[17] Y. C. Kwon, J. Lee and S. K. Sul, "Extending operational limit of IPMSM in signal-injection sensorless control by manipulation of convergence

point," *IEEE Trans. Ind. Appl.*, vol. 55, no. 2, pp. 1574-1586, Mar./Apr. 2019.

[18] J. Lee, Y. C. Kwon and S. K. Sul, "Signal-injection sensorless control with tilted current reference for heavily saturated IPMSMs," *IEEE Trans. Power Electron.*, vol. 35, no. 11, pp. 12100-12109, Nov. 2020.

[19] T. Tuovinen and M. Hinkkanen, "Adaptive Full-Order Observer With High-Frequency Signal Injection for Synchronous Reluctance Motor Drives," *IEEE Trans. Emerg. Sel. Topics Power Electron.*, vol. 2, no. 2, pp. 181-189, Jun. 2014.

[20] A. Varatharajan, G. Pellegrino and E. Armando, "Signal-Injection Sensorless Control of Synchronous Reluctance Machines for Overload Operation," *IEEE Trans. Power Electron.*, vol. 37, no. 5, pp. 5874-5883, May 2022.